

Emission-Line Datacubes of the HH 32 Stellar Jet

PATRICK HARTIGAN,¹ LYNNE A. HILLENBRAND,² MATUEZ MATUSZEWSKI,³ ARLINDO CHAN BORGES,⁴
JAMES D. NEILL,³ D. CHRISTOPHER MARTIN,³ PATRICK MORRISSEY,³ AND ANNA M. MOORE⁵

¹*Physics and Astronomy Dept., Rice University, 6100 S. Main, Houston, TX 77005-1892*

²*Department of Astronomy, MC 249-17, California Institute of Technology, Pasadena, California 91125*

³*Cahill Center for Astrophysics, California Institute of Technology, 1216 East California Boulevard, Pasadena, California 91125*

⁴*Department of Astronomy, MC 249-17, California Institute of Technology, Pasadena, California, 91125*

⁵*Research School of Astronomy and Astrophysics, Australian National University, Canberra, ACT 2611, Australia*

ABSTRACT

We analyze datacubes of over 60 emission lines in the HH 32 stellar jet acquired with the Keck Cosmic Web Imager (KCWI). The data cover the less-explored blue portion of the spectrum between 3586Å and 6351Å, and have both high spectral ($R \sim 10000$) and spatial ($\lesssim 1''$) resolution. The study includes all three major ionization states of oxygen, three Balmer lines, multiple lines of Fe II and Fe III, as well as the first datacubes ever acquired for important unblended diagnostic lines such as He II $\lambda 4686$, Ca I $\lambda 3933$, and Mg I] $\lambda 4571$. The data cubes generally sort according to excitation, and have a relatively continuous progression from the highest-excitation ions (He II, O III) through the intermediate-excitation ions (O I and H I) to the lowest-excitation ions (Ca II and Mg I). Merging the KCWI cubes with HST images leads to several new insights about the flow, including evidence for bow shocks, partial bow shocks, spur shocks, Mach disks, jet deflection shocks, a wiggling jet, and potential shock precursors.

The most surprising result is that one of the velocity components of Fe II in the Mach disk suddenly increases in flux relative to other lines by a factor of two, implying that the Mach disk vaporizes dust in the jet. Hence, jets must accelerate or entrain dust to speeds of over 300 km s^{-1} without destroying the grains.

Keywords: Herbig-Haro objects (722), Stellar Jets (1607), Shocks (2086), Astrophysical dust processes (99)

1. INTRODUCTION

Since their discovery in the 1950's as nebulous emission-line objects in the vicinity of dark clouds, HH-objects have become a primary tool for investigating outflows associated with star formation. The observed radial velocities and similarity to supernova remnant spectra led [Schwartz \(1975\)](#) to identify HH objects as radiatively-cooled zones in shock fronts, and deep emission-line images revealed that these shocks generally occur within highly-collimated jets driven from young stars (e.g. [Mundt & Fried 1983](#)). Typically denser than their surroundings, stellar jets can alter the morphologies of their surroundings radically as they penetrate large distances into their ambient clouds (e.g. [McGroarty et al. 2004](#)). Together with radiation from the star, jets provide a means for young stars to energize clouds against gravitational collapse, and significantly reduce the masses of the resultant stars in some simulations ([Hansen et al. 2012](#)). Most current models launch stellar jets from magnetized accretion disks, and jets provide one of the only ways to study this phenomenon. These flows remove angular momentum from the disks (e.g. [Nolan et al. 2017](#)), with implications for the formation of gaps in disks and planetary migration at the earliest times.

Beacuse HH jets radiate emission lines and are optically thin, they are especially well-suited to the standard non-LTE analyses of interstellar medium physics. For example, one can measure electron densities, temperatures, and ionization states from the observed emission line ratios, though these quantities are averages over the entire emitting region being observed. Most HH objects are resolved spatially, and with the subarcsecond resolution afforded by HST images it is possible to resolve the cooling distances behind individual shock waves in many cases. Velocities are high enough to enable

proper motion studies for each emission feature across an entire flow with a temporal baseline of $\lesssim 10$ years, and with radial velocities as broad as several hundred km s^{-1} in some objects one can perform emission-line analysis both spatially and as a function of velocity (i.e., within a data ‘cube’ with two spatial dimensions and a third dimension in velocity). When combined with proper motion data, the only unmeasured coordinate in phase space for these flows is the line-of-sight distance, and even that can be inferred to some degree for simple geometries.

This wealth of quantitative data has led to several insights concerning jets and the sources that drive them (see [Frank et al. 2014](#), for a recent review). Jets from young stars become collimated within ~ 100 AU of their source, and emerge with typical opening angles of ~ 5 degrees (e.g. [Reipurth et al. 2000](#); [Hartigan & Morse 2007](#)). They move radially from their driving stars, but often appear to ‘wiggle’ as the flow from the source changes in direction or if the source itself undergoes orbital motion ([Masciadri & Raga 2002](#)). The main cause of shock waves in jets is velocity variability, and many jets consist of a series of nested bow shocks along the axis of the flow ([Hartigan et al. 2001](#); [Lee et al. 2016](#)). This geometry naturally produces faster material along the axis of the jet and slower flow along the periphery (e.g. [Cerqueira et al. 2015](#)). Quasi-stationary X-ray knots located within a few hundred AU of the source may be related to the jet collimation process or to boundary set up between a stellar wind and a disk wind ([Günther et al. 2014](#)).

Within jets, emission line ratios imply shock velocities typically range from 30 km s^{-1} to 80 km s^{-1} , with higher values present in bright bow shocks. Cooling distances measured from high-spatial resolution observations imply magnetic fields must provide the main source of pressure in cooling zones, and lead to measurements of Alfvénic Mach numbers of a few ([Hartigan & Wright 2015](#)). When velocity pulses brush up against slower material along the edge of the jet, an oblique ‘spur’ shock propagates into the surrounding material, and when the jet drives a bow shock it forms a Mach disk that decelerates the shock and becomes visible as a compact knot situated near the apex of the bow shock, often with a distinct signature in the kinematics and emission-line ratios ([Hartigan et al. 2011](#)). Occasionally a stronger shock redirects a jet if the flow encounters a dense obstacle such as a molecular cloud (e.g. HH 110; [Reipurth et al. 1997](#); [Raga et al. 2002](#)), while intersecting shocks

may produce short-lived hot spots known as Mach stems (Hartigan et al. 2016). These modes of shock production have inspired several recent laboratory experiments which attempt to observe how readily a given type of shock forms and to follow as it evolves with time (e.g. Frank et al. 2014).

Among the first group of HH objects to be cataloged by Herbig (1974), HH 32 is unusual both in that it is one of the few sources that has high-excitation lines such as [O III] 5007 (Brugel et al. 1981), and in that the brightest knots are redshifted (Dopita 1978). The jet emanates from the primary star, AS 353A, in a pre-main-sequence binary pair. AS 353A has broad, bright emission lines with classic P-Cygni type absorption features that vary with time (Mundt & Fried 1983; Hartigan et al. 1986). The source is surrounded by molecular gas (Edwards & Snell 1983), at a distance of ~ 410 pc according to Gaia Collaboration (2016). The bright emission-line knots HH 32A and HH 32B possess large linewidths and exhibit profile differences in $H\alpha$, [S II] and [O III] that were among the first objects to be modeled successfully as bow shocks (Solf et al. 1986; Hartigan et al. 1987). The first subarcsecond resolution images of the region from HST uncovered a wealth of filamentary structures and knots along the flow, and the observed proper motions showed that the jet must be aligned close to the line of sight (Curiel et al. 1997). Data cubes of several optical emission lines in the region around HH 32A were published by Beck et al. (2004), who constructed a bow shock model for each of the bright knots in the cube (see also Raga et al. 2004). Davis et al. (1996) also explained the observed low-velocity H_2 emission associated with knots A and B with a model where the molecular gas was confined to the extreme wings of a bow shock.

In this paper we use the new Keck Cosmic Web Imager (KCWI) to acquire datacubes of the entire redshifted portion of the HH 32 outflow, including HH 32A, HH 32B, HH 32D, and the emission between HH 32D and AS 353A. The spectra cover the blue portion of the optical between [O II] $\lambda\lambda 3727$ and [O I] $\lambda 6300$, and have both high spectral ($R \sim 10000$) and spatial ($\lesssim 1''$) resolution. Emission lines in the blue spectral region are fainter than standard red tracers such as $H\alpha$ and [S II] $\lambda\lambda 6720$, but the blue has many more emission lines and can trace elements and ionization states that are inaccessible in the red. In what follows we describe the data acquisition and reduction techniques in Sec. 2, and present the results of the data cubes in Sec. 3. Sec. 4 combines the existing HST

images with the new KCWI cubes to construct a summary model for the entire region, including the location of the major shock waves along the flow and a discussion of their consequences in terms of the observed line profiles and line ratios. We bring together our conclusions in Sec. 5.

2. DATA ACQUISITION AND REDUCTION

Observations of HH32 were obtained with the Keck Cosmic Web Imager (KCWI; [Morrissey et al. 2018](#)), an integral field spectrograph mounted on the Keck II telescope, on 14 June, 2017, during the third commissioning run for the instrument. The small slicer with a field of view $20'' \times 8.25''$ was used along with the BM grating, giving a resolution of $R \approx 10,000$. Three separate central wavelengths were used for the observations: 4020 Å (blue), 4700 Å (green), and 5950 Å (red) which gives some amount of overlap between the blue and green cubes. For each wavelength configuration, there were two on-target exposures and an adjacent-in-time offset sky exposure, all of duration 600 sec. Due to a rising moon, the blue cube was acquired first, followed by green and then red. The instrument position angle was set to 105° in order to roughly align the field with the outflow axis. Flux calibration was achieved using nearby-in-time observations of the spectrophotometric standard BD+25°4655.

Data cube processing generally followed the procedures described in Section 4 of [Morrissey et al. \(2018\)](#). In summary, bias frames, internal lamp exposures including arc lines, continuum flat and continuum bars exposures, and external dome flats were acquired the morning after the science observations were taken. The arc lamp and the continuum bars exposures are used to define the geometry of the raw data, while the continuum flats and the dome flats are used to correct illumination non-uniformities.

Once the geometry has been defined and the illumination has been corrected, the sky exposures were used to define a sky model using basis splines that accurately follow the sky spectrum as a function of wavelength. This results in a low-noise sky model that is then subtracted from each science image. Offset sky observations were used since the filling factor of object light in the on-target observations was a large fraction of the KCWI FOV, causing over-subtraction if the sky were modeled from the on-target observations.

The slicer design of KCWI means that the ends of each cube are subject to nonuniformity in the spatial-spectral coverage, resulting in banding in the reduced cubes with approximately 20% of the nominal wavelength range of the cubes affected. Fortunately, the blue and green cubes overlap sufficiently such that there is no loss in wavelength coverage, while there is a real gap between the reduced green and red cubes. For our data set, the effective total wavelength coverage is 3586Å–5136Å and then 5540Å–6351Å.

Following processing, the two on-target exposures for each of the three wavelength ranges were averaged, and the three cubes were then spatially registered. This involved fitting two-dimensional gaussians to the $H\gamma$ line in the blue and green cubes, the $H\beta$ line in the green cube, and the O I 6300Å line in the red cube so as to determine the peaks. The three cubes were then aligned and trimmed to encompass the same spatial area.

The full cubes have a native pixel asymmetry, with 0.34'' pixels in the “x” direction from the individual image slices, and 0.1457'' pixels in the “y” direction on the detector. Each cube was resampled to square pixels by binning by a factor of three in the y-direction and regridding in x-direction to yield 0.437'' pixels in each dimension, which sufficiently subsamples the 0.7-1.0'' seeing conditions during the observations while still providing good signal-to-noise in the fainter lines.

In most cases we want to examine how the brightness of a specific emission line varies spatially and with velocity, and then compare its datacube with those of different lines. To extract a datacube for one line, we first rebin the data from its dispersion of 0.25 Å per pixel to a cube that spans -150 km s^{-1} to 600 km s^{-1} centered on the rest wavelength of the emission line in the frame of reference of AS 353A. The LSR velocity of AS 353A is $+8 \text{ km s}^{-1}$ from molecular line surveys (Edwards & Snell 1983).

Although observing in the blue part of the spectrum opens up opportunities to study many fainter lines that have been to date largely ignored, this innovative aspect to the data set is also in a sense a weakness in that KCWI detects enough lines that in a number of cases the broad velocity extent of the HH 32 outflow causes them to blend. Even though emission lines are optically thin in HH shocks, it is not possible to deblend lines reliably if they arise from different elements. However, we were

able to deblend the [O II] 3726.03Å and [O II] 3728.82Å lines, separated in velocity by 225 km s⁻¹, in the following manner. Because the electron densities inferred from the red [S II] lines in HH 32 (e.g. [Brugel et al. 1981](#); [Beck et al. 2004](#)) are typically a factor of five higher than the critical densities for [O II] λ3726 and [O II] λ3729 ($\lesssim 70 \text{ cm}^{-3}$), the flux ratio between these [O II] lines will be g_3A_{31}/g_2A_{32} , where subscripts 3, 2, and 1 refer respectively to the $^2D_{3/2}$, $^2D_{5/2}$, and $^4S_{3/2}$ levels of [O II], and the 3-1 and 2-1 transitions are λ3726.03 and λ3728.82, respectively. Using the atomic parameters compiled by [Mendoza \(1983\)](#), in the high density limit $I_{3726}/I_{3729} = 2.88$. Because there is no emission blueward of -30 km s^{-1} , we can use the 3726.03Å profile to trace the velocity range of -60 km s^{-1} through $+195 \text{ km s}^{-1}$. Likewise, there is no emission redward of $+450 \text{ km s}^{-1}$, so we use the 3728.82Å profile scaled by 2.88 for velocities greater than $+225 \text{ km s}^{-1}$. At intermediate velocities the known separations and flux ratios suffice to solve for the profile shape.

Finally, terrestrial emission lines are not always subtracted perfectly in the data reduction procedure. We corrected for residual sky lines in the relevant data slices by fitting a spline to the emission along the slit, using the pixels at top and bottom of the datacube to measure sky. This procedure worked well for [O I] λ6300, but failed for [O I] λ5577, where the night sky line residuals are too large and variable. The high-velocity portions of the [O I] λ5577 cube are unaffected by the residual night sky, but show no significant differences from the [O I] λ6300 cubes at those velocities. Most of the data reduction beyond the standard pipeline reductions, such as extracting data cubes of individual lines, deblending data cubes, and improving sky subtraction were done with various routines in IRAF.

3. EMISSION LINE ANALYSIS

3.1. System Overview

Fig. 1 presents an overview of the HH 32 jet and shows the extent of the KCWI images. The background r-band (F675W) image in this figure was taken with HST on 25 Aug, 1994 as part of program GO-5367 (PI: Raymond). Throughout the paper we use HST images from this program as a guide to what the structure of the jet looks like at high spatial resolution. However, we must

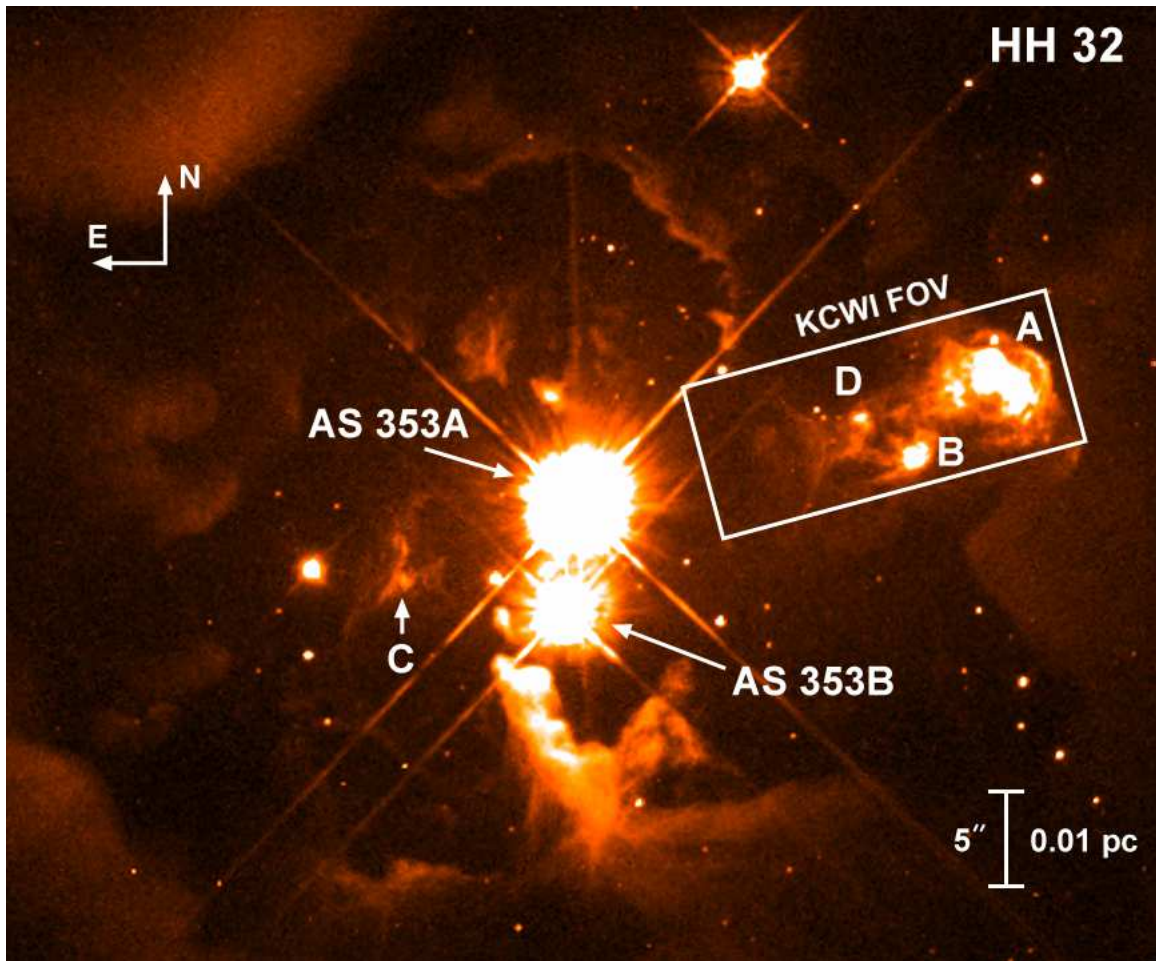


Figure 1. Overview of the HH 32 Jet and its exciting star AS 353A, showing the spatial coverage and orientation ($PA = 105^\circ$) of the new KCWI data cubes superposed upon an archival r-band image from HST that includes $H\alpha$ and the red $[S\ II]$ lines. The scale bar assumes a distance of 410 pc (Gaia Collaboration 2016). The bright jet knots A, B, and D are all redshifted, while knot C (not observed by KCWI) is blueshifted. The nebulous structures not labeled as part of the jet are reflection nebulae. The jet is oriented close to the line of sight.

bear in mind that in the 25 years since the HST data were acquired the jet knots have moved $\sim 1'' - 2''$ away from AS 353A, and differential motions within the jet will shift features relative to one another by up to an arcsecond (Curiel et al. 1997). The differential motions are on the order of the ground-based seeing and do not affect how we interpret images, though one cannot expect a perfect correspondance between what we observe today and what appears in the HST images from 1994.

The environs of AS 353A and AS 353B are quite remarkable. Reflection nebulae in the HST image outline an intricate cavity shape around the binary pair. Within the jet, knot A splits into two main components, each appearing like a bow shock in the images and each showing the broad emission and spatial separations of high- and low-velocity emission expected from a simple bow shock model (Beck et al. 2004). Knot B occurs along the edge of the flow and also resembles a bow shock in existing spectral maps (Beck et al. 2004), while knot D has a more extended arcuate shape visible in the Balmer lines of H. Much structure appears in both the $H\alpha$ and red [S II] HST images as well as in their difference image (Fig. 2). The framework for interpreting such images is described in Hartigan et al. (2011) - filamentary Balmer lines designate the shock fronts, and forbidden line emission such as from [S II] follows in a spatially-resolved cooling zone. We discuss each of the bright knots in detail in Sec. 4.

3.2. *KCWI Datacubes of Emission Lines*

Our three wavelength settings detected over 60 emission lines in HH 32 (Tables 1 and 2). Mesa-Delgado et al. (2009) catalogued a large number of emission lines in their comprehensive study of HH 202 in Orion, and many of these also occur in HH 32, though we do not see the Orion H II recombination lines in our data. Eliminating the faintest lines, blends, and lines where a portion of the emission profile is lost off the end of the CCD, we are left with 27 emission lines that have their own data cubes. Lines from the same element and ionization state often appear identical, so we can combine these to increase the signal-to-noise in the final products (Table 1).

We group the final data cubes approximately according to excitation, with the highest-excitation cubes (He II, Ne III and O III) in Fig. 3, the next group (He I, Fe III, N II and O II) in Fig. 4, the third set (H I and O I) in Fig. 5, and the lowest-excitation group (S II, Fe II, Ca II and Mg I) in Fig. 6. We take ‘excitation’ to be a sum of the energy needed to ionize the atom to the ionization state of interest, plus the excitation of the level above ground. For example, He II 4686 requires 24.6 eV to ionize He I to He II, plus another 51 eV to populate the upper state of the transition.

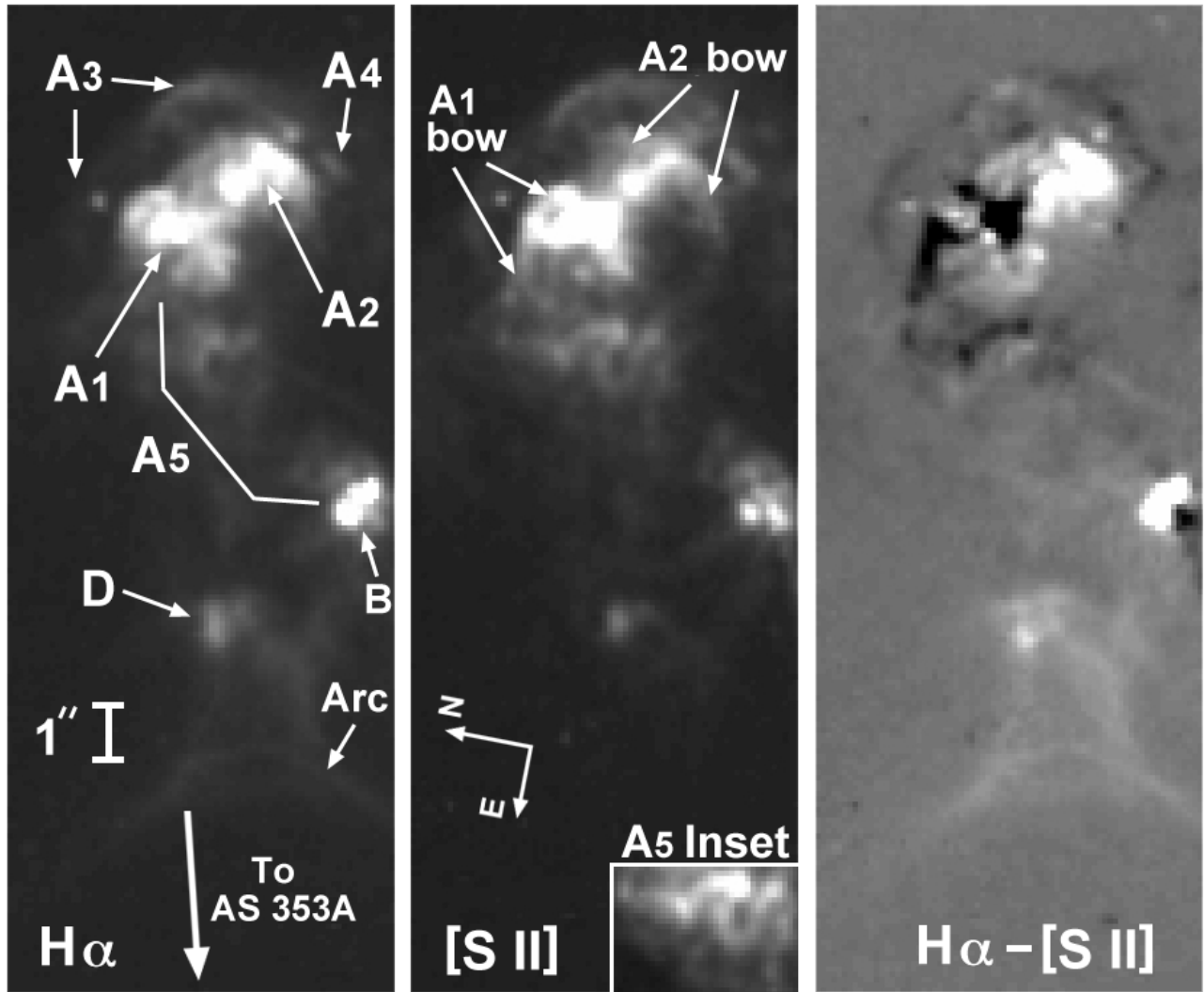


Figure 2. Narrow-band HST images in $H\alpha$ (F656N; left) and $[S\ II]$ (F673N; center) and a difference image (right) of the HH 32 jet for the region of the KCWI observations shown in Fig. 1. The scale bar of $1''$ corresponds to 410 AU. The knot nomenclature follows that of Beck et al. (2004). The inset of feature A5 is scaled to highlight the sinuous jet at that location.

Similarly, $[O\ III]\ 5007$ needs 35.1 eV to doubly-ionize oxygen, plus another 2.5 eV to populate the upper state. On the other hand, it makes sense to group $[O\ I]\ 6300$ with the $H\ I$ Balmer lines (~ 11 eV) because the ionization state of oxygen is tied to that of hydrogen through a large charge exchange coefficient (Williams 1973).

Figs. 3 - 6 show that lines with roughly the same excitation generally have very similar-looking data cubes. It is probably easiest to see differences in the cubes by looking carefully at the emission

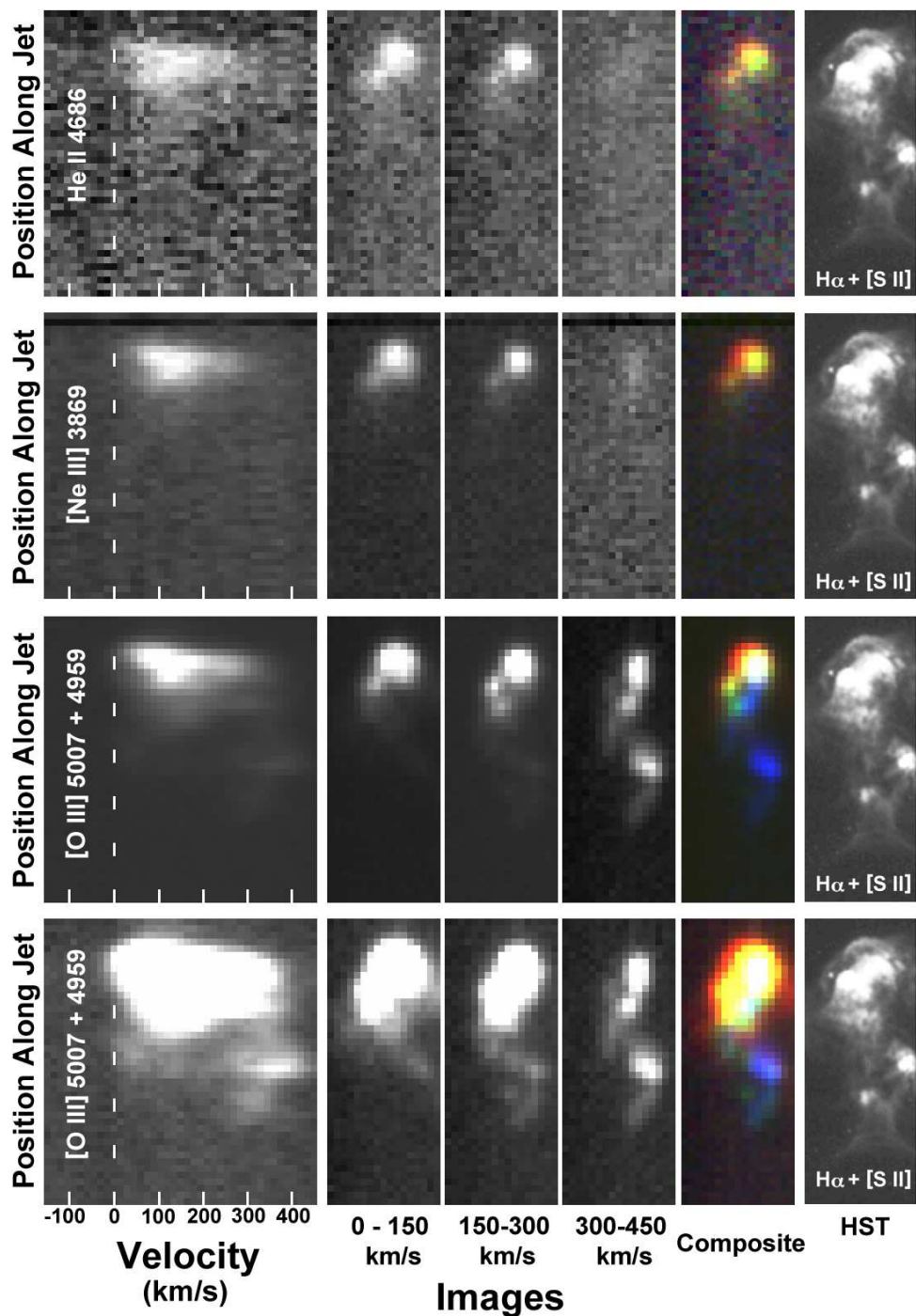


Figure 3. KCWI data cubes of the highest-excitation lines: He II 4686, [Ne III] 3869, and [O III] 5007+4959. Left: position-velocity diagrams coadded across the width of the jet. The jet moves from the bottom to the top in the figure. Center: Velocity images summed over 150 km s^{-1} intervals. Right: Color composite of the redshifted jet, where the red, green, and blue channels are taken from the slowest ($0 \text{ km s}^{-1} - 150 \text{ km s}^{-1}$), intermediate ($150 \text{ km s}^{-1} - 300 \text{ km s}^{-1}$), and fastest ($300 \text{ km s}^{-1} - 450 \text{ km s}^{-1}$) images, respectively. Far right: HST r-band image in Fig. 1. Two scalings are shown for [O III] 5007+4959.

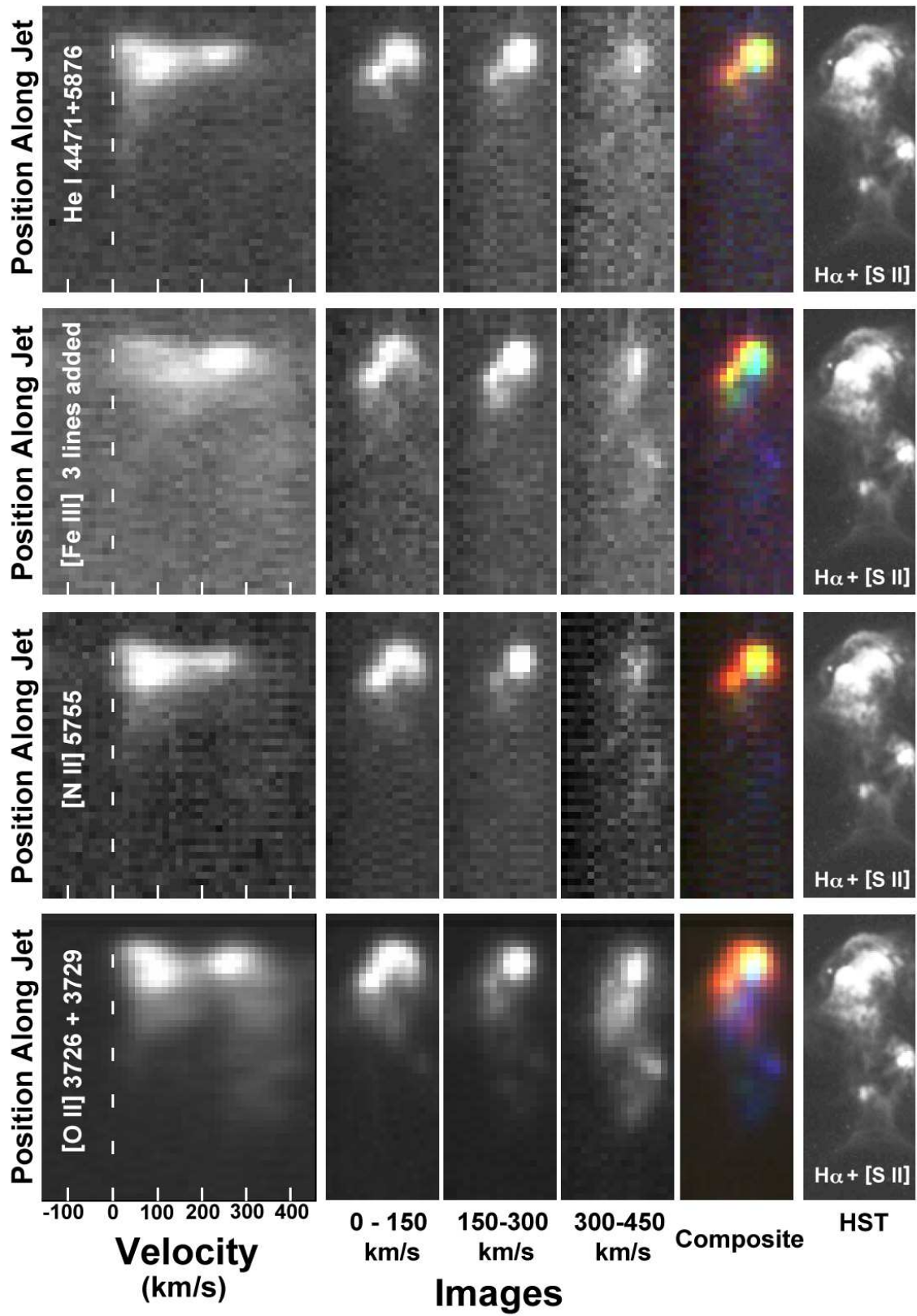


Figure 4. Same as Fig. 3 but for the intermediate/high-excitation lines: He I 4471+5876, [Fe III] 4755+4770+4987, [N II] 5755, and [O II] 3726+3729.

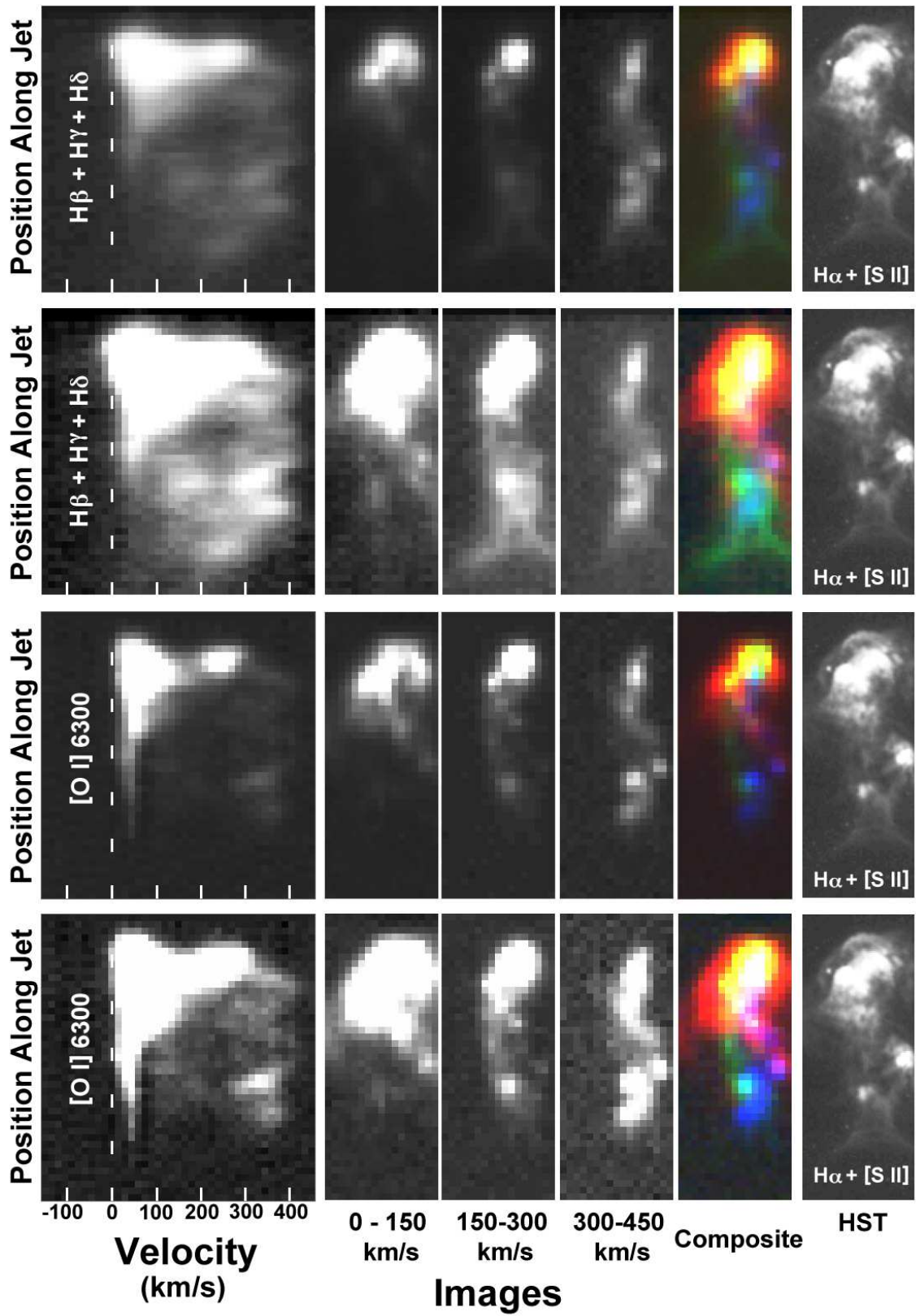


Figure 5. Same as Fig. 3 but for H I ($H\beta + H\gamma + H\delta$) and $[O I] \lambda 6300$. Two scalings are shown for each line in order to highlight structure in both the brightest and faintest parts of the diagrams.

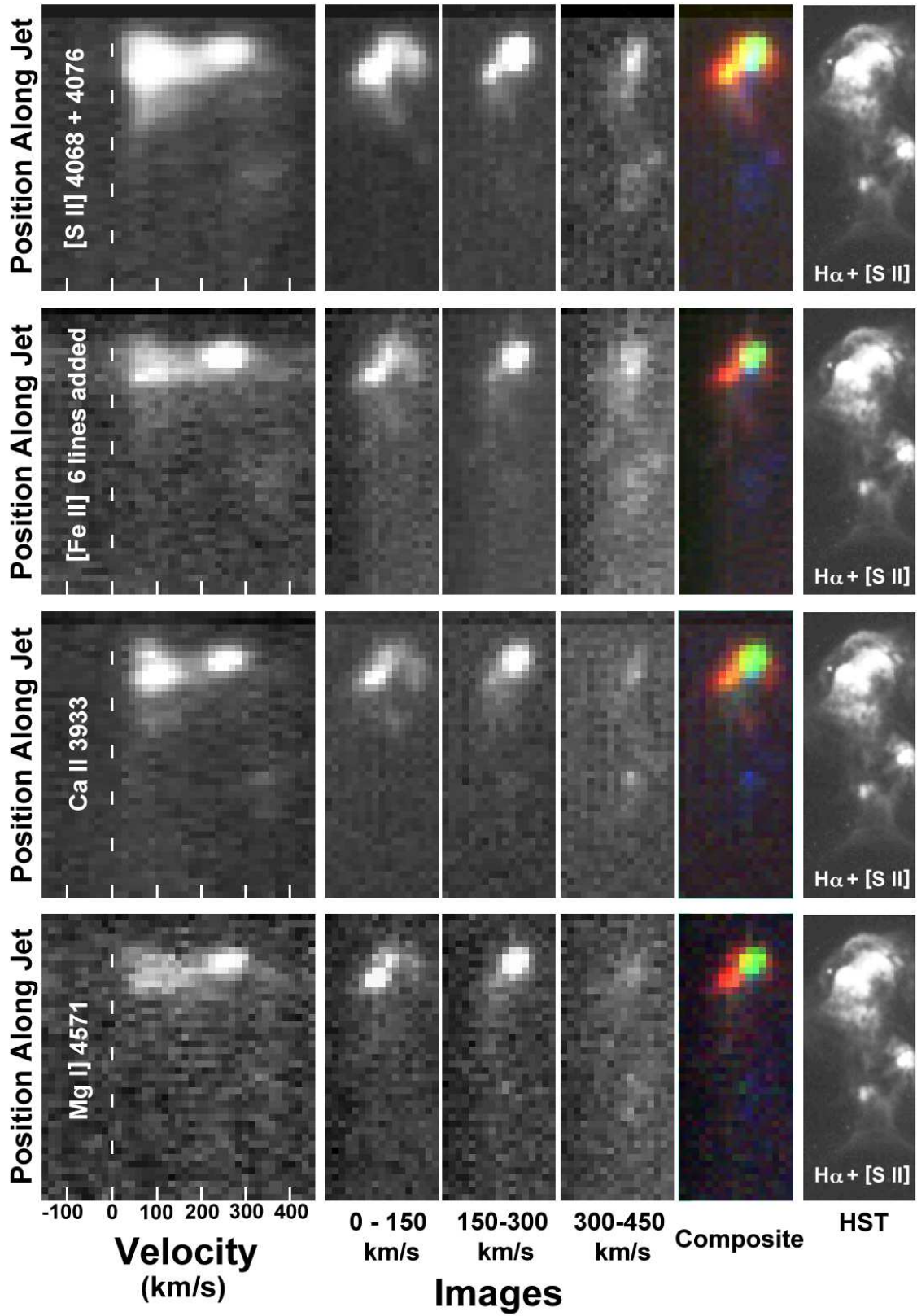


Figure 6. Same as Fig. 3 but for the lowest-excitation lines: [S II] 4068+4076, [Fe II] 4244+4287+4815+4890+4905+5112, Ca II (K) 3933, and Mg I] 4571.

Table 1. Bright Emission Lines Included in a Datacube

Line	Figure	Line	Figure	Line	Figure	
H β	4861.33	5	[O II] 3726.03 ^c	4	[Fe II] 4243.97 ^d	6
H γ	4340.47 ^a	5	[O II] 3728.82 ^c	4	[Fe II] 4287.39	6
H δ	4101.74	5	[O III] 4958.91	3	[Fe II] 4814.55	6
He I	4471.47	4	[O III] 5006.84	3	[Fe II] 4889.68	6
He I	5875.64	4	[Ne III] 3868.75	3	[Fe II] 4905.37	6
He II	4685.70 ^b	3	Mg I] 4571.10	6	[Fe II] 5111.65	6
[N II]	5754.64	4	[S II] 4068.60	6	[Fe III] 4658.10	4
[O I]	6300.30	5	[S II] 4076.35	6	[Fe III] 4701.62	4
			Ca II 3933.66	6	[Fe III] 4881.00	4

a: Observed in both green and blue cubes

b: Blend of 5 lines in a 26 km s⁻¹ interval

c: [O II] 3726+3729 are blended, but can be combined into a single cube (see text)

d: Possibly blended with very weak [Fe II] 4244.85

from knots A1 and A2 near the top of the low-velocity (0 km s⁻¹ – 150 km s⁻¹) images. Emission in the high-excitation cubes comes mainly from the leading knot A2, while knot A1 is the brighter of the two in the low-excitation cubes. This difference also appears in the position-velocity diagrams. Two emission lines with roughly the same level of excitation ought to produce similar data cubes in shock-excited gas, and this correspondence is indeed what we observe in the KCWI spectral cubes.

3.3. Reddening, Ionization and Velocity in the Jet

Ratios of the H γ /H β and H δ /H β cubes are unremarkable, and show roughly constant values across all regions of bright emission. The observed values of 0.31 ± 0.03 for H γ /H β and 0.14 ± 0.015 for H δ /H β agree well with previously observed values of 0.298 and 0.162, respectively (Brugel et al. 1981). Balmer line ratios in high-velocity shocks like those in HH 32 should resemble those expected from Case B recombination (Hartigan et al. 1987), so in principle we can use the Balmer line ratios to estimate reddening. Using a standard extinction law and taking Balmer ratios at 10⁴ K (tables 7.2

Table 2. Other Lines Detected

<i>Faint Lines, Not Included in a Datacube</i>					
H-10	3797.90	[Ar IV] 4711.37	[Fe II] 4276.83	[Fe II] 4457.95	[Fe II] 5746.97
H-9	3835.39	[Ar IV] 4740.16	[Fe II] 4346.85	[Fe II] 4728.10	[Fe III] 4754.83
He I	4921.93	[S III] 6312.10	[Fe II] 4474.91	[Fe II] 4774.75	[Fe III] 4769.90
He I	5015.68	[Fe II] 4114.48	[Fe II] 4452.10	[Fe II] 4973.42	[Fe III] 4987.20
<i>Blends</i>					
H-8 3889.05 + He I 3888.65		[O III] 4363.21 + [Fe II] 4359.33			
[O I] 5577.37 + Night Sky		[Fe II] 4416.27 + [Fe II] 4413.76			
Ca II (H) 3968.47 + [Ne III] 3868.75 + H-7 3970.07					
<i>Lines Detected, But Not Fully Mapped By KCWI</i>					
[N I] 5200.26	[O I] 6363.78	[Fe II] 5527.34	[Fe II] 5158.03	[Fe II] 5158.80	
[N I] 5197.90					

and 4.4 of [Osterbrock 1989](#)), we estimate the logarithmic extinction at $H\beta$, $C_{H\beta} = 1.38 \pm 0.30$ from the $H\gamma/H\beta$ ratio, and $C_{H\beta} = 1.41 \pm 0.25$ from $H\delta/H\beta$. For comparison, [Brugel et al. \(1981\)](#) found $C_{H\beta} = 1.05 \pm 0.07$ using the ratio of transauroral to auroral [S II] lines, a method that is superior to ours in that it spans a much larger wavelength range, although flux calibrations for the faint near-infrared [S II] lines can be challenging. These estimates all imply a rather large reddening along the line of sight to HH 32; for example, $C_{H\beta} = 1.38$ implies $A_V \sim 2.75$.

Our data are particularly good for delineating the ionization structure in the flow because we simultaneously acquired deep data cubes of emission lines from three ionization states of oxygen, [O I] $\lambda 6300$, [O II] $\lambda\lambda 3726+3729$, and [O III] $\lambda\lambda 5007+4959$. We present these cubes side-by-side in Fig. 7. Several trends are worth noting here. First, the [O I] emission generally covers a broader area perpendicular to the jet, as expected for a flow that moves nearly along our line of sight (e.g. [Beck et al. 2004](#)). Second, the A5 area in the middle of the frame (cf. the middle panel of Fig. 2) emits

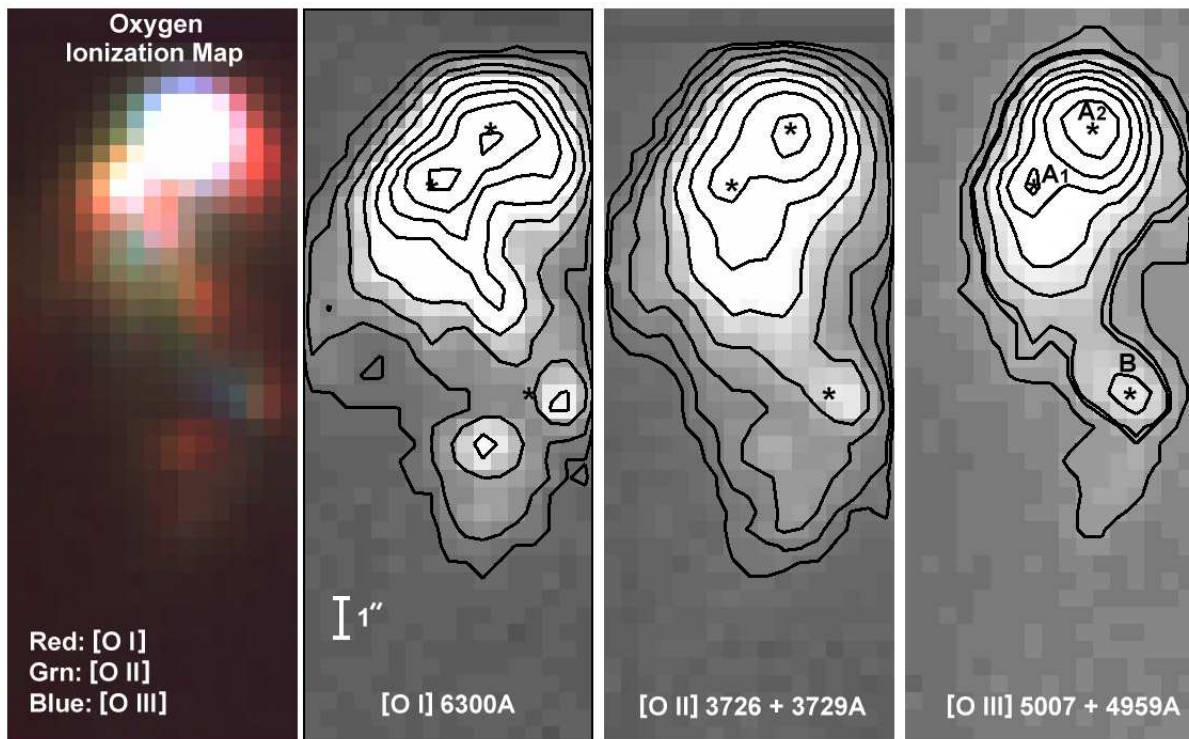


Figure 7. Oxygen ionization composite. Contours are drawn in factors of $\sqrt{3}$ in surface brightness. Each pixel is $0.437''$. The asterisks denote the peak intensities of knots A1, A2 and B in the [O III] 5007+4959 image, and are useful for identifying excitation gradients.

strongly only in [O I], consistent with it being bright in the [S II] HST image, where it appears as a wiggling jet. Finally, there is a strong decrease in the ionization from left to right in knot B as one moves from the center of the jet to closer to the edge of the flow, as highlighted by the positional offset between the asterisk that marks the [O III] peak from the peak contours in the [O I] image. Analogous offsets in knots A1 and A2 are small. There is also a low-ionization knot about $2''$ to the left of knot B in Fig. 7, but this knot and the emission below it have very high radial velocities of $\gtrsim 300 \text{ km s}^{-1}$ (Fig. 5).

Fig. 8 maps the average Balmer line radial velocities throughout the region by integrating over the line profile shape at each point (the equivalent of a moment-one map in molecular data). There is a broad area of low radial velocity gas that surrounds the outflow, with the fastest material located along the axis of the flow. Such behavior has been seen before in this jet (Beck et al. 2004), and is consistent with a series of bow shocks viewed nearly along the line of sight.

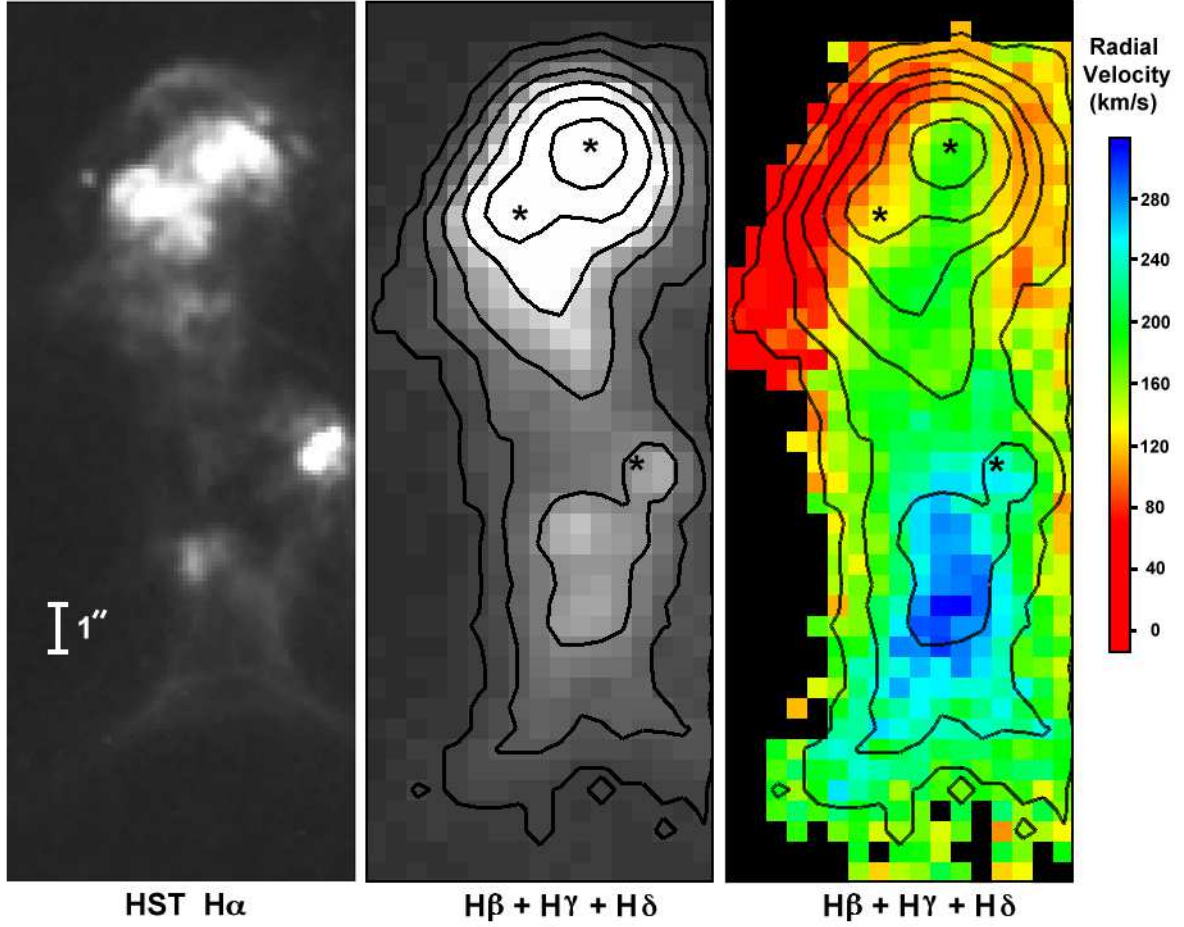


Figure 8. Left: HST image at H α . Center: Combined H β + H γ + H δ image. Adjacent contours differ by a factor of $\sqrt{3}$ in flux. Right: Average velocity relative to AS 353A in the summed H β + H γ + H δ composite. Asterisks denote the peak emission of knots A1, A2, and B in Fig. 7.

Animations provide a much better way to follow the complex velocity structure in this outflow (Fig. 9). We created a movie of the H I datacube for the on-line version of the paper that cycles through the radial velocities between -60 km s^{-1} to $+450 \text{ km s}^{-1}$ in 15 km s^{-1} intervals. Moving from blue to red, significant emission first begins around -30 km s^{-1} with a curved filament of emission near the apex of the bow shock A3 (refer to Fig. 2 for knot names and orientations). By 0 km s^{-1} this emission intensifies to form a flattened knot above (downstream from) the location of the peak of A2, with a wing to the emission to the left ahead of A1. The right side of knot B also appears, with a weak extension into the A5 region between B and A1. Between 0 km s^{-1} and 60 km s^{-1} , the emission associated with knot A3 shifts down (upwind) and gets somewhat narrower. At this

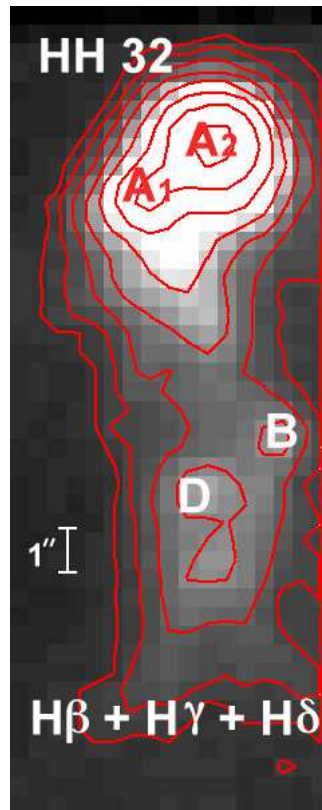


Figure 9. Animation through the velocity frames of the KCWI datacube at $H\beta + H\gamma + H\delta$. The animation moves through each frame between -60 km s^{-1} through $+450 \text{ km s}^{-1}$ in 15 km s^{-1} intervals. The greyscale placeholder image is integrated over the the full velocity range, and has contours spaced by a factor of $\sqrt{3}$ in flux that provide a reference throughout the animation. The video duration is 12 seconds.

point the emission is a bright crescent that aligns with the velocity-integrated peaks of A1 and A2. Between 60 km s^{-1} and 120 km s^{-1} knot A has begun to split into its two distinct components, A1 and A2. A5 continues to brighen, and by 105 km s^{-1} knot D first appears just as the emission shifts from the right side of knot B to its left side. Knots D and B now bracket the sides of the jet.

As we continue the journey through the cube, we move from the low-velocity gas to the intermediate-velocity gas in Fig. 5. By 180 km s^{-1} , emission from both knots B and D have shifted more towards the axis of the flow, and the ‘Arc’ feature labeled in Fig. 2 at the bottom of the cube has begun to appear. This feature emits in Balmer lines, but not in the forbidden lines. Emission from the A5 region has now shifted to the left, and is located directly upstream of A1. Both A1 and A2 knots are distinct peaks, and align on the maximum contours of the integrated cube. Between 180 km s^{-1}

and 240 km s^{-1} the emission from knots B and D merges into a single feature down the axis of the flow, and the ‘Arc’ at the bottom of the cube nearest to AS 353A is clearly visible. Knot A1 has all but disappeared, but knot A2 remains bright. The A5 emission shifts back to the right, aligned with the center of the flow. At the high end of the intermediate velocities, 240 km s^{-1} to 300 km s^{-1} , the merging of knots B and D produces a bright knot at 300 km s^{-1} along the axis of the flow that is visible both in the contours of the integrated intensity and in the velocity map (Fig. 8). A faint bridge now connects this emission to a knot in A5, connecting in turn to A2, where its peak has shifted down (upwind) of the integrated contour peak by about $0.6''$.

Between 300 km s^{-1} and 360 km s^{-1} the knots of A5 and A2 merge into a single linear feature centered on the jet’s axis and located upstream from the peak emission of knot A2. Emission along the axis between knots B and D remains strong. The north side of knot B reappears as an emission source around 360 km s^{-1} . Above 360 km s^{-1} , emission along the jet gradually fades, and disappears by 420 km s^{-1} . Knot B remains visible to slightly higher velocities, and all emission is gone by 450 km s^{-1} . The full complexity of the outflow is on display in Figs. 10 through 12, where we plot the spectra of various lines for each pixel. Fig. 12 presents a similar spectral map for the region around knot B. We discuss these maps more in the next section.

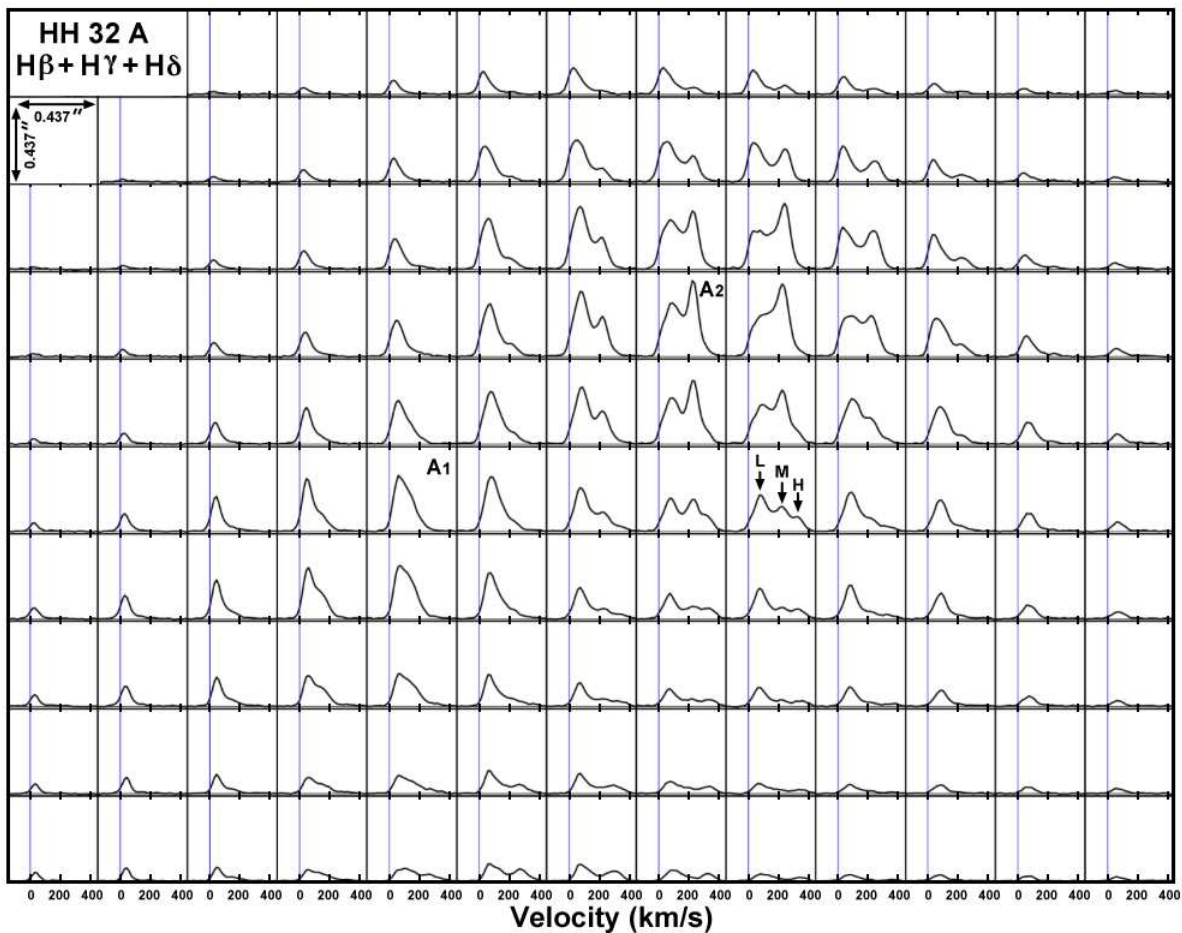


Figure 10. Spectral map across HH 32 in $H\beta + H\gamma + H\delta$. Labels mark the locations of the knots A1 and A2 as defined in the [O III] image (Fig. 7). The three distinct velocity components labeled ‘L’, ‘M’, and ‘H’ merge into two components at knot A2. The low-velocity component surrounds the entirety of the emission.

4. DISCUSSION

Even though the spatial and velocity structures within HH 32 are complex, we can understand most of what we observe in the HST images and in the KCWI datacubes by using the standard picture of a highly supersonic jet with a variable direction and speed. Fig. 13 depicts how the jet should appear if it were viewed perpendicular to the direction of the flow. To construct this figure to scale, we stretched the HST image along the axis of the jet to account for a viewing angle of 20 degrees to the line of sight as inferred from proper motion measurements (e.g., Fig. 10 of Curiel et al. 1997). Fig. 13 labels the major features along the flow, indicates the shapes of the main shock waves, depicts

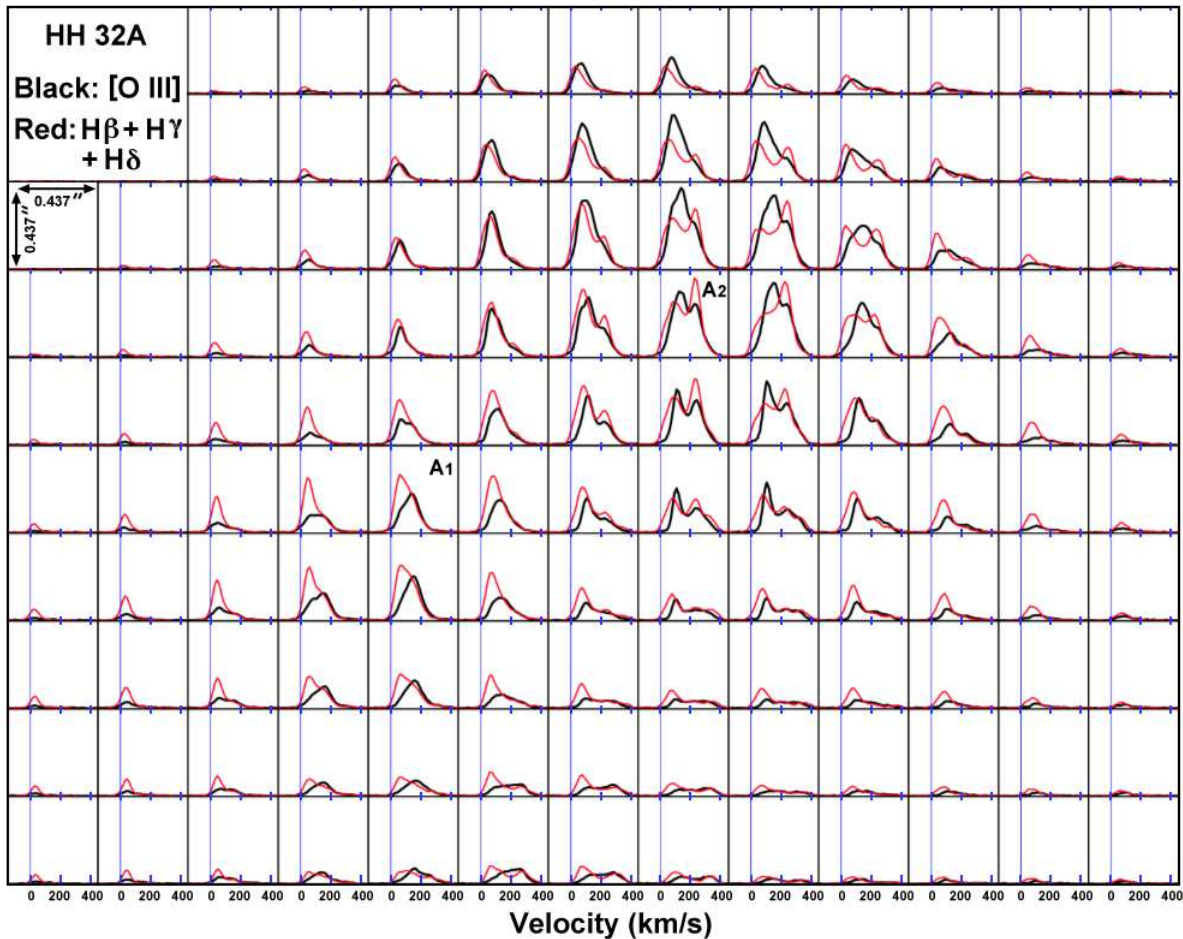


Figure 11. Same as Fig. 10 but superposing the [O III] line profiles on top of the H I line profiles.

whether or not the shocks occur in ambient (or very slowly moving) gas or in the jet, and outlines an approximate boundary between the jet flow and the surrounding medium.

The following section describes the observational evidence to support the scenario drawn for each of the features in Fig. 13, keeping in mind the inherent limitations imposed by the lack of axial symmetry in the flow. The location of the boundary between the jet and ambient material is often uncertain, as the gas typically only becomes visible as it passes through a shock front, so not all portions of the flow are traced by the emission line observations.

4.1. Schematic for the HH 32 Redshifted Jet

The Arc - Weak Shocks in the Jet:

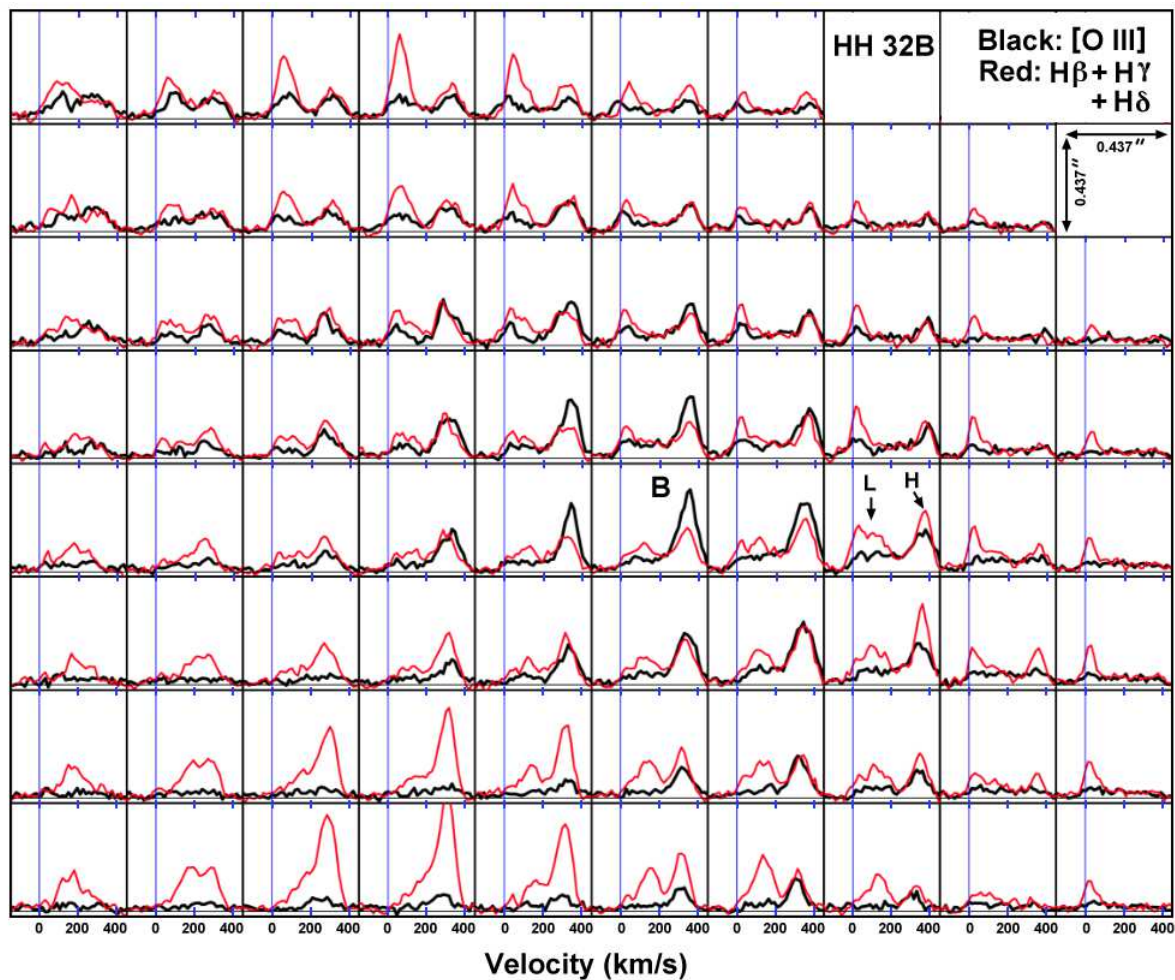


Figure 12. Same as Fig. 10 but for the area around knot B. The location of knot B, defined by the peak of the [O III] emission, is marked.

The structure labeled ‘Arc’ in Fig. 2 is the closest emission line feature to AS 353A in the redshifted jet. The HST images show only $H\alpha$ and no [S II] at this location, though the Arc is visible faintly in the HST narrowband [N II] $\lambda 6583$ image of Curiel et al. (1997). The Arc appears only in our Balmer composites with KCWI and not in [N II] $\lambda 5755$ line or in any of the other forbidden lines, though [N II] $\lambda 5755$ is one of the fainter lines in our cubes (Fig. 4). The radial velocity in the Balmer lines is high in Fig. 5, about 250 km s^{-1} . The emission line morphologies and velocities all imply that the Arc is a weak shock in the jet. Linewidths are narrow, there are no bright knots to define a cooling zone, and radial velocities are high.

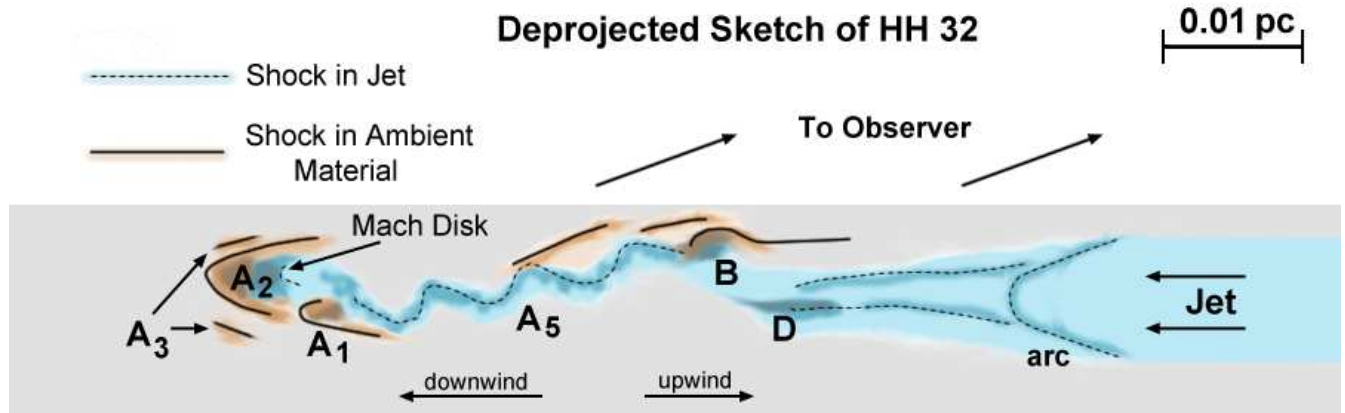


Figure 13. A heuristic model for the HH 32 system, viewed perpendicular to the flow direction. The position of the features derives from deprojecting the HST images using an observing angle of 20 degrees to the line of sight. Blue colors indicate jet material and orange colors indicate ambient gas, with the shock waves in those materials depicted by dashed lines and solid lines, respectively. The major features of the jet are labeled. The jet flows from right to left. The driving source AS 353A would be located well off the frame (~ 0.045 pc) to the right of this diagram (Fig. 1.)

The simplest explanation for the Arc is that the feature forms as a pulse of faster material overtakes slower material in the jet. In this scenario, the Arc represents a weak bow shock which forms as 250 km s^{-1} pulse overtakes somewhat slower gas ahead of it. This model predicts the Arc will have a high proper motion, similar to the other features in the redshifted jet.

If the Arc has no proper motion, it probably represents a focusing shock. These oblique shocks occur as the jet responds to a sudden increase in the ambient density, or if the jet ‘overexpands’ and the ambient medium redirects the jet back towards its axis. The concept is similar to the focusing-cavity jet model of Cantó (1980), with the important difference that the external medium collimates a spherical flow from the source in the Cantó model, whereas here the flow must already be collimated when it encounters the Arc because the Arc subtends a small solid angle as viewed from the driving source AS 353A. The continuum HST image (Fig. 1) shows that the AS 353 binary is embedded within a dark cloud and appears to have evacuated a cavity in the cloud. With this geometry it is plausible that a jet would burrow through a cloud along its path, and focusing shocks would mark

the location where the jet enters the cloud. However, this scenario only works if the Arc has no proper motion.

Knot D - Another Jet Pulse:

In the HST images, knot D is a bright linear feature situated a bit to the left of the axis of the flow in Figs. 2 and 13. A faint filament of $H\alpha$ emission precedes knot D along the the jet. The KCWI composites look somewhat different, with, for example, the integrated [O I] image showing a knot aligned to the axis of the jet (Fig. 7). Taken at face value, it means that knot D has formed forbidden lines at its apex in the 25 years since the Hubble images. The datacubes show an increase in velocity along the center of the jet (Sec. 3.3). All of these observations are consistent with a jet pulse of $\sim 300 \text{ km s}^{-1}$ that overtakes material in front of it. The velocity difference between this pulse and the one in front of it must be $\lesssim 100 \text{ km s}^{-1}$ to account for the lack of [O III] emission in Fig. 7.

Knot B - Partial Bow Shock into a Cavity Wall:

Together with knots A1 and A2, knot B is one of the brightest features in HH 32 and has plenty of [O III] emission. Hence, it must represent a strong shock wave. The HST image shows two or three compact knots, depending on the emission line. The knot is located on the southern boundary of the jet (Fig. 1), and as noted in Sec. 3.3 and Fig. 7, there are strong ionization and velocity gradients in this area, with both velocity and excitation increasing towards the axis of the jet. The r-band HST image (Fig. 1) shows what appears to be a spur shock into the surrounding gas, and the velocity of that material is low, a few tens of km s^{-1} (Figs. 8 and 12, Sec. 3.3).

Knot B has all the hallmarks of a partial bow shock moving into ambient material. Its location along the edge of the flow means a shock will encounter ambient gas there, and the wing of the bow shock becomes the spur shock into the ambient gas. Weak shocks in the ambient molecular gas then produce the H_2 emission observed along the interface between the jet and the ambient gas by Davis et al. (1996). Spectral maps of the knot B region show distinct low-velocity and high-velocity components (labeled ‘L’ and ‘H’, respectively in Fig. 12) over the entire area. The low-velocity material extends to the side of the jet beyond the high-velocity material. [O III] is brightest in the high-velocity gas where its emission peaks at the location of knot B. In a bow shock model, this

emission arises from the apex of the bow ($\sim 330 \text{ km s}^{-1}$), while the Balmer line emission distributes more evenly across the bow and results in more of a double-peaked emission line profile (e.g. [Solf et al. 1986](#); [Hartigan et al. 1987](#)). The northern side of the bow (left side in Figs. 2, 8 and 12 and down in Fig. 13), is replaced by weaker shocks which serve to deflect the flow away from the cavity. These shocks produce emission only at high velocities, as is observed. In fact, one can connect the fastest portion of the jet in [O I] $\lambda 6300$ from the northern side of knot B all the way to the Mach disk in knot A2 (Fig. 5).

The partial bow shock model described above does not explain the multiple knots in the HST images. Shock velocities over 200 km s^{-1} like those present in knot B are prone to cooling instabilities that could form knots (e.g. [Suzuki-Vidal et al. 2015](#)), or the flow may simply be clumpy on size scales of a few hundred AU. Ground-based datacubes such as ours do not have enough spatial resolution to probe the velocity structures of features on these size scales.

A5 - Wiggling Jet Projected Along the Line of Sight:

Region A5 connects knot B to knots A1 and A2. The [S II] HST image has a remarkable morphology of 3 – 4 sharp bends that resemble a rope dropped onto the floor. Velocities here are among the highest in the jet (Sec. 3.3). The sinuous feature emits in [O I], [O II], and [O III]. It is difficult to trace exactly where the jet goes near A1. The velocity images (Figs. 3 – 6) show the highest velocity material turns back to the south near A1 and connects seamlessly with knot A2. The $H\alpha$ datacubes of [Beck et al. \(2004\)](#) enjoyed $0.5''$ seeing, and show a separate faint knot at 395 km s^{-1} with weak bow-like tails on either side at this location. Our Balmer slice also shows this feature, though we are unable to make out the wings. This is the region where the jet feeds into the main bow shock at A2.

We identify the sinuous feature with a wiggling jet. Such structures are common in HH flows, and typically emit only in low-excitation lines as they are excited by weak internal shocks. Deprojecting the flow shows that one can fit ~ 4 sinusoidal variations with modest amplitudes in a jet between knot B and knot A1 and still have that portion of the jet project onto one small area of the sky (Fig. 13). Hence, the severe bends present in the image of the A5 jet result from a projection angle nearly along the line of sight.

Overall, the kinematics and morphology of A5 are well-explained by a simple wiggling jet viewed nearly along the line of sight. The strong [O III] in this region is unusual however (Fig. 3). To understand why this occurs we would need an HST-resolution image at [O III] and attempt to analyze the shock waves at each position along the jet. One other unusual aspect of the A5 region is the presence of extensive low-velocity gas in the spectral maps, especially in the Balmer lines (component ‘L’ in Figs. 12 and 10). The HST difference image in Fig. 2 hints as to what this emission might be: a Balmer-only filament exists downwind from knot B and connects to the wiggling jet in A5. This feature is likely to be a weak shock that propagates into the ambient material to provide a ‘sheath’ of low-velocity Balmer emission that surrounds the jet (the ‘spur’ shock drawn in region A5 in Fig. 13). The faint H₂ emission in this area can also arise from these weak shocks (Davis et al. 1996).

Knot A1 - Classic Bow Shock:

Beck et al. (2004) found they were able to explain the velocity and spatial structure of the bright knot A1 in their H α cubes remarkably well with a simple bow shock model. Our new datacubes fully support their interpretation. The spectral maps of A1 have an extended low-velocity halo that surrounds the high-velocity peak, and the [O III] emission peaks at a higher radial velocity than the Balmer lines do. All of these features agree with the predictions of bow shocks viewed nearly along the line of sight (Beck et al. 2004; Raga et al. 2004).

The region is rather complex in the HST images. As noted above in the discussion of A5, a fast jet knot is superposed about 0.5'' to the south of the brightest part of A1, presumably on its way to A2. The bright knot in A1 is in the correct location to be a Mach disk, but it is hard to know for certain because the apex of the bow shock also projects to this location at this orientation, and the rest of the region, including the A1 bow shock, is quite clumpy on small spatial scales. The [O III] emission peaks at around 150 km s⁻¹ in knot A1 (Fig. 11), so this is what the velocity of the working surface should be, and will also be the shock velocity because this knot appears to move into ambient gas. Bow shocks need not have Mach disks for episodic flows, because if the jet shuts off the Mach disk will vanish while the bow shock continues to propagate.

Knot A2 - Bow Shock with a Mach Disk:

Knot A2 shares many of the same characteristics as knot A1, including a bright, compact, high-velocity and high-excitation core surrounded by a low-velocity halo. Fig. 2 shows A2 has an extended bow shock, but the brightest knot in the region is very compact, and not clearly resolved even with HST. Both the location of this knot relative to the putative bow shock and the fact that it aligns with the fastest part of the jet in A5 support its identification as a Mach disk.

The kinematics of the flow also support a Mach disk interpretation for the object. Fig. 10 shows three distinct velocity components in the Balmer lines labeled L, M, and H, where component L surrounds the entire flow as a low-velocity sheath. As the jet moves downwind into knot A2, component H at $\sim 325 \text{ km s}^{-1}$ vanishes and the flux in component M at $\sim 230 \text{ km s}^{-1}$ suddenly rises. We interpret this 230 km s^{-1} value as the velocity of the working surface, in which case the Mach disk would have a shock velocity of $\sim 100 \text{ km s}^{-1}$.

Knots A3 and A4 - Possible Lateral Radiative Precursor:

Feature A3 actually consists of two arcs, one located just beyond A1 and another associated with A2. Along the southern edge of the flow, A3 continues with a feature known as A4 (Fig. 2). Although A3 and A4 seem to lie downwind of knots A1 and A2, Fig. 13 shows that this situation is not necessarily the case for a viewing angle near to the line of sight. The radial velocities in A3 and A4 are near zero (Fig. 8), and in fact these areas have a bit of blueshifted emission, and appear in the -30 km s^{-1} slices. Linewidths in this region are typically $\lesssim 50 \text{ km s}^{-1}$. These regions also have narrow H_2 emission at the ambient velocity, though the spatial resolution of the H_2 observations makes it difficult to tell if the emission comes from A3 and A4 or the downwind edges of A1 and A2 (Davis et al. 1996).

A radiative or magnetic precursor is an attractive model for A3 and A4 because one would expect the precursor to follow the overall outline of the main shock, but retain a linewidth close to the thermal speed and have little radial motion. For the orientation of HH 32, the precursor could lie along the side of the jet and still appear to be projected ahead of it. HH 32 is one of the few HH outflows with high enough shock velocities to expect to see a radiative precursor. Effectively the shock front creates a small H II region that follows it along on its journey. This phenomenon has been observed in the bright HH knot HH 2A', which also emits strongly in [O III] (Hartigan et al.

2011). If the precursor idea is correct, A3 and A4 should have the same proper motions as the high-excitation knots A1 and A2. If the radiative precursor is bright enough, it will cause fluorescence in H_2 that may be observable at $2.12\mu\text{m}$.

It is also possible that A3 and A4 represent the edges of a cavity evacuated by a previous ejection, and a weak shock propagates into the ambient gas at these locations. Though there is no evidence for a larger scale outflow, if we take the velocity of the bow shock A2 to be 230 km s^{-1} and the deprojected distance of knot A2 from AS 353A to be 0.12 pc (Fig. 1), the travel time of knot A2 to its current location is only about 500 years, 3 – 4 orders of magnitude shorter than the likely age of the star. Hence, knot A2 is almost certainly not the first ejection from the system, though it could still propagate into ambient gas if the outflow is sufficiently time variable that the ambient medium refills the jet cavity between major outbursts.

Overall, the simple scenarios outlined above are remarkably successful in explaining most of the complexities in our data cubes. However, the HST images remind us to not be overconfident, as there are many overlapping knots and filaments that become resolved on subarcsecond scales. To address that level of detail scientifically would require combining high-dispersion spectra on these spatial scales with temporal observations that can distinguish internal proper motion differences. Such observations are beyond what we can do in the present work, and could be difficult to interpret owing to the orientation of this outflow, which essentially projects the entire jet onto a small area.

4.2. Spectroscopic Evidence for Dust Destruction

The spectral maps of the low-excitation lines ([Fe II] and [S II] composites, Ca II $\lambda 3933$ and Mg I] $\lambda 4571$) in the region of knot A1 and A2 in Figs. 14, 15, and 16 are generally quite similar. However, one discrepancy stands out sharply: the velocity component we identify as belonging to the Mach disk of knot A2 has a larger [Fe II]/[S II] ratio by a factor of two relative to that in the low-velocity component and throughout the profiles in the rest of the region. This enhancement is not present in the Ca II/[S II] ratio, and appears only weakly in Mg I]/[S II].

The easiest way to explain the enhanced Fe II flux in knot A2 is if the shock waves there convert iron dust grains into gas. Dust grains can be destroyed in shocks both by grain-grain collisions

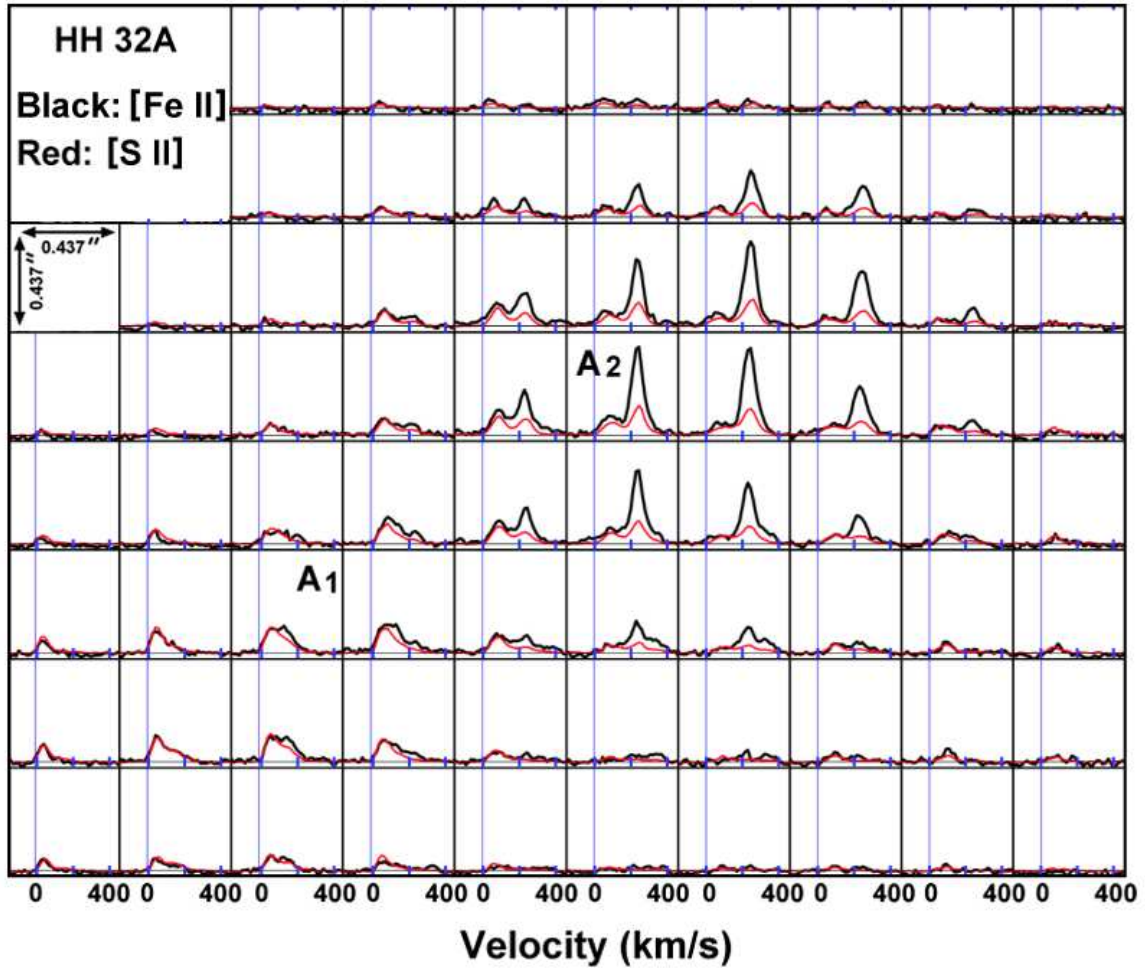


Figure 14. Spectral map of the knot A region, superposing the [Fe II] line profiles on top of the [S II] line profiles. These lines should track one-another closely; however, the data show a marked increase in one-velocity component in the [Fe II] lines at knot A2 which we interpret as evidence for dust destruction, where the shock releases refractory elements into the gas phase.

and through sputtering by atoms and ions (see [Jones 2004](#), for a review). Shattering by grain-grain collisions breaks large grains into smaller pieces for impact velocities as low as 1 km s^{-1} ([Jones et al. 1996](#)), but this process simply changes the size distribution of the grains without modifying the gas to dust mass ratio unless the impact velocities exceed the vaporization threshold of $\sim 20 \text{ km s}^{-1}$ ([Tielens et al. 1994](#)). Above about 50 km s^{-1} , sputtering dominates dust destruction and converts $\sim 50\%$ of the mass of an iron grain into gas for injection velocities $\gtrsim 170 \text{ km s}^{-1}$ (Fig. 11 of [Jones et al. 1996](#)), and a similar fraction for C and Si grains (Fig. 7 of [Slavin et al. 2015](#)). In the case of

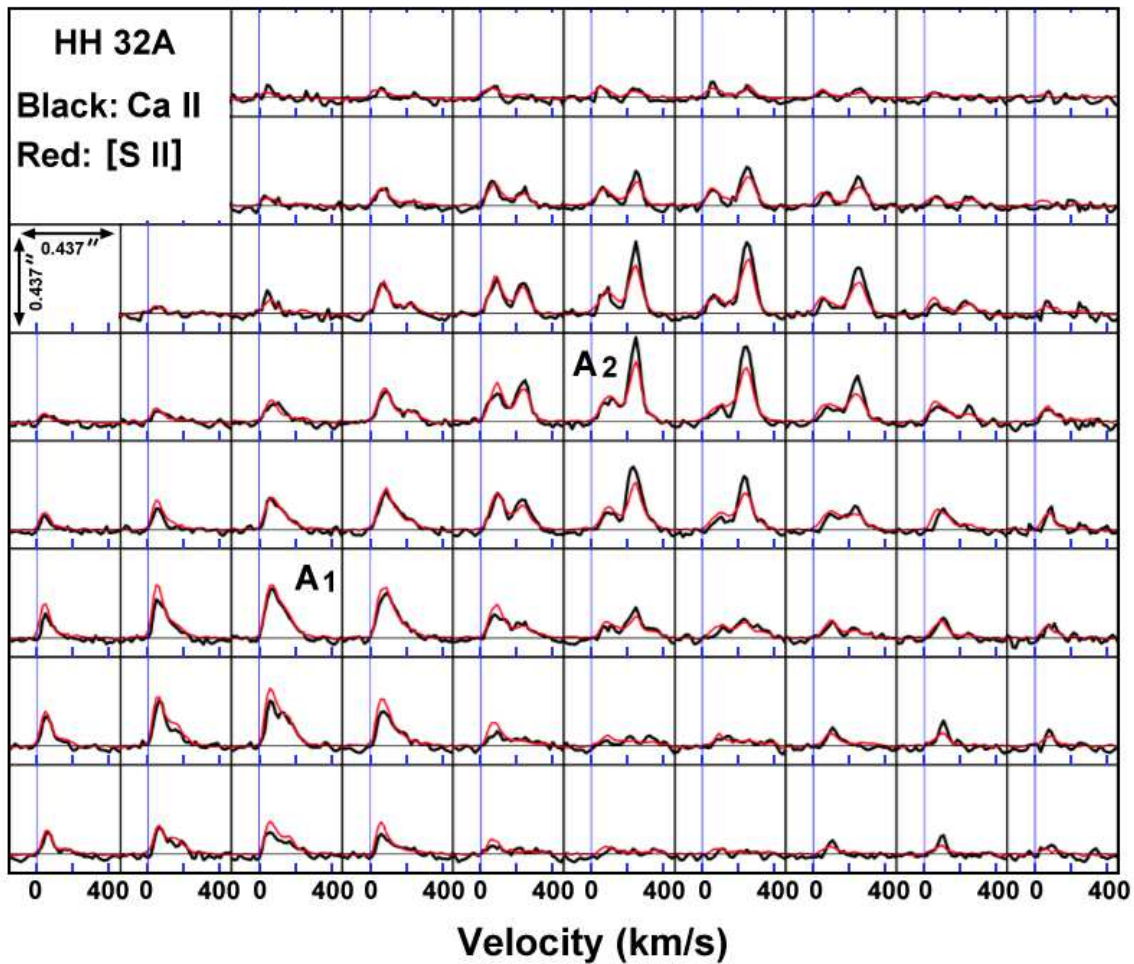


Figure 15. Same as Fig. 14 but for Ca II $\lambda 3933$. There are no systematic differences between the [S II] and Ca II line profiles.

knot A2, the shock wave is a fairly strong one, with a shock velocity $\sim 100 \text{ km s}^{-1}$ if it is the Mach disk and $\sim 230 \text{ km s}^{-1}$ if it is the apex of the bow shock. In either case such a strong shock could substantially increase the gas phase abundance of iron at this location. Iron is highly refractory, and some evidence exists for its depletion in jets (Antoniucci et al. 2014). Our data seem to be the first direct evidence for a refractory element being returned to the gas phase by a shock in a stellar jet, however.

5. CONCLUSIONS

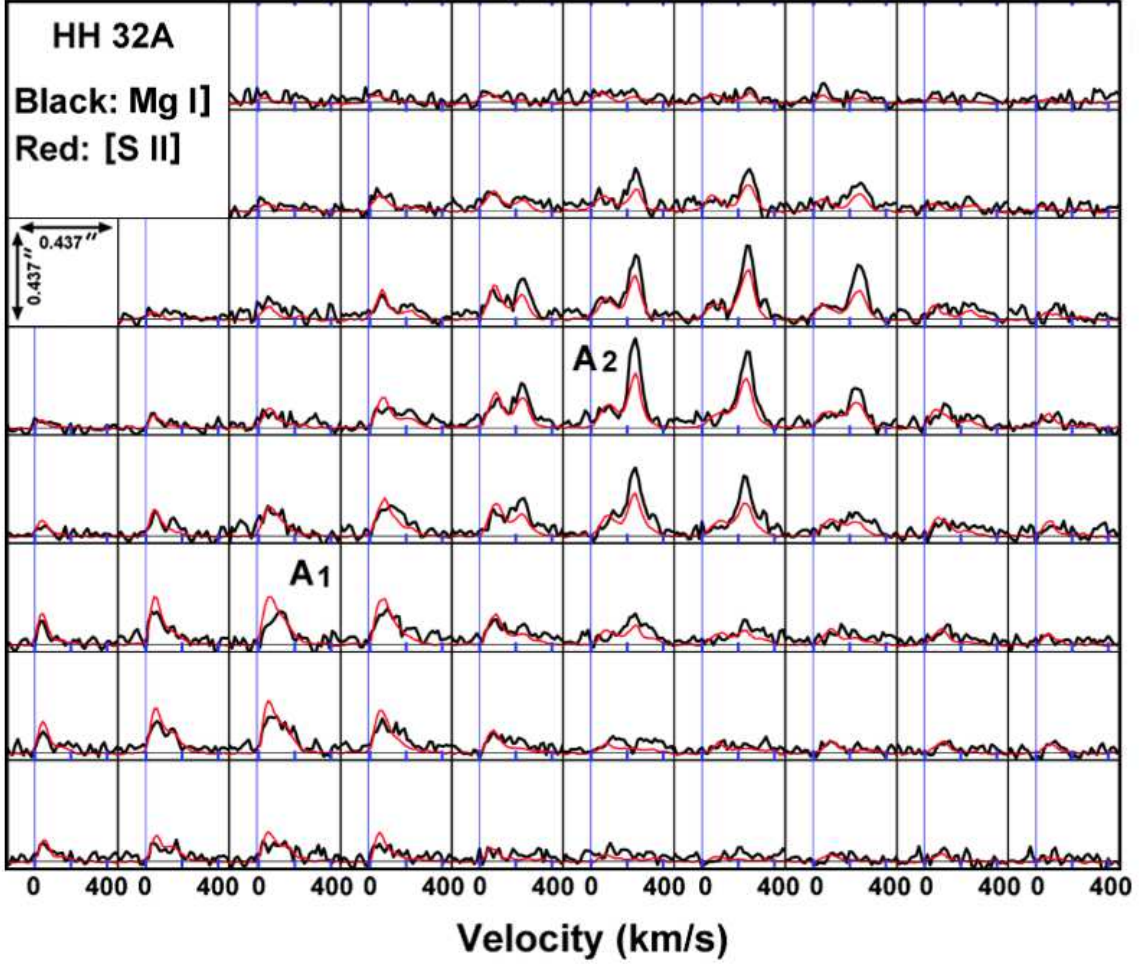


Figure 16. Same as Fig. 14 but for the Mg I] 4571 line.

In this paper we have acquired and analyzed over 60 datacubes of the stellar jet HH 32. The cubes have $\sim 30 \text{ km s}^{-1}$ velocity resolution and $\lesssim 1''$ seeing. The project focused on blue lines, which enables the first detailed study of several new ionization states of common elements in stellar jets, including datacubes of Ca II, Mg I, O I, O II, O III, He I, He II, Fe III, Fe II, S II, N II, and three Balmer lines. We found that the overall morphologies of the line emission within these cubes sort remarkably well when grouped according to excitation, defined as a combination of the ionization potential of the element and the energy level of the upper state above ground.

The results generally agree with previous works in the areas of overlap, and fit well with a scenario of a pulsed jet with variable ejection angle that we view nearly along line of sight. Knots A1 and A2 exhibit all the kinematic and excitation signatures expected for a resolved bow shock. Bright

areas in these regions are likely to be Mach disks where jet material enters a working surface. The A1 and A2 bows are fed by A5, a high-velocity wiggling jet. Closer to the source, knot B appears to be a partial bow shock, while knots D and a feature known as the Arc are shocks within the jet material. The spectral cubes of the Mach disk in knot A2 show a sudden jump in the [Fe II] flux that we attribute to an increase of iron in the gas phase as a result of dust destruction in that shock. A similar jump is absent in Ca II and only weakly visible in Mg I]. Dust could have been entrained into the flow, or even launched in the jet from its circumstellar disk, although in these scenarios the dust would have to survive being accelerated to over 300 km s^{-1} without being destroyed. The extended low-velocity filaments A3 and A4 that appear ahead of the main bow shocks could identify a magnetic or radiative precursor to the main shocks, or may represent the walls of a cavity formed by a previous ejection.

These observations show the power (and challenges) of combining high-spectral resolution datacubes of many lines with narrow-band HST images. Without spectral information, it is easy to misinterpret HST images owing to projection effects, even when multiple filters are available. Alternatively, data cubes taken with ground-based resolution blur the geometry, leading to simplistic interpretations that change markedly once fragments and filaments become resolved. The blue spectral region has the advantage of being able to acquire velocity cubes in O I, O II, and O III, and also samples both very high-excitation lines (e.g. He II $\lambda 4686$) and very low-excitation lines (e.g. Mg I] $\lambda 4571$). A downside is that there are enough lines that blends begin to become a problem, though one can deblend the [O II] doublet reliably under most circumstances.

ACKNOWLEDGMENTS

We thank Luca Rizzi for his participation in these KCWI commissioning observations. This work has made use of data from the European Space Agency (ESA) mission *Gaia* processed by the *Gaia* Data Processing and Analysis Consortium. Funding for the DPAC has been provided by national institutions, in particular the institutions participating in the *Gaia* Multilateral Agreement.

Facilities: Keck (KCWI)

REFERENCES

- Antoniucci, S., La Camera, A., Nisini, B.,
Giannini, T., Lorenzetti, D., Paris, D., & Sani,
E. 2014, *A&A* 566, 129
- Beck, T. L., Riera, A., Raga, A. C., & Aspin, C.
2004, *AJ* 127, 408
- Brugel, E. W., Böhm, K.-H. & Mannery, E. 1981,
ApJS 47, 117
- Cerqueira, A. H., Vasconcelos, M. J., Raga, A. C.,
Feitosa, J., & Plana, H. 2015, *AJ* 149, 98
- Cantó, J. 1980, *A&A* 86, 327
- Curiel, S., Raga, A., Raymond, J.,
Noriega-Crespo, A. & Cantó, J. 1997, *AJ* 114,
2736
- Davis, C. J., Eisloffel, J., & Smith, M. D. 1996,
ApJ 463, 246
- Dopita, M. 1978, *ApJS* 37, 117
- Edwards, S. E., & Snell, R. 1983, *ApJ* 270, 605
- Frank, A., et al. 2014, in *Protostars and Planets*
VI, H. Beuther, R. Klessen, C. Dullemond & T.
Henning eds. (Tucson:Univ. of Arizona Press)
- Gaia Collaboration; Prusti, T., et al. 2016, *A&A*
595, A1
- Günther H. M., Li, Z.-Y., & Schneider, P. C. 2014,
ApJ 795, 51
- Hartigan, P., Frank, A., Foster, J. M., Wilde, B.
H., Douglas, M., Rosen, P. A., Coker, R. F.,
Blue, B. E., and Hansen, J. F. 2011, *ApJ* 736, 29
- Hartigan, P., Foster, J., Frank, A., et al. 2016,
ApJ 823, 148
- Hartigan, P., Mundt, R. & Stocke, J. 1986, *AJ* 91,
1375
- Hartigan, P., & Morse, J. A. 2007, *ApJ* 660, 426
- Hartigan, P., Morse, J. A., Reipurth, B.,
Heathcote, S., & Bally, J. 2001, *ApJ* 559, L157
- Hartigan, P., Raymond, J. & Hartmann, L. 1987,
ApJ 316, 323
- Hartigan, P., & Wright, A. 2015, *ApJ* 811, 12
- Hansen, C. E., Klein, R. I., McKee, C. F., &
Fisher, R. T. 2012, *ApJ* 747, 22
- Herbig, G. H. 1974, *Lick Obs. Bull.* 658, 1
- Jones, A. P. 2004, *Astrophysics of Dust*, ASP
Conf. Ser. 309, 347
- Jones, A. P., Tielens, A. G. G. M. & Hollenbach,
D. J. 1996, *ApJ* 469, 740
- Lee, C.-F., Hirano, N., Zhang, Q., Shang, H., Ho,
P. T. P., & Mizuno, Y. 2016, *ApJ* 805, 186
- Masciadri, E., & Raga, A. C. 2002, *ApJ* 568, 733
- McGroarty, F., Ray, T. P., & Bally, J. 2004, *A&A*
415, 189
- Mendoza, C. 1983, *IAU Symp.* 103, 143
- Mesa-Delgado, A., Esteban, C., Garca-Rojas, J.,
Luridiana, V., Bautista, M., Rodriguez, M.,
López-Martín, L., & Peimbert, M. 2009,
MNRAS 395, 855
- Morrissey, P., Matuszewski, M., Martin, D. C.,
Neill, J. D. et al. 2018, *ApJ* 864, 93
- Mundt, R., & Fried, J. *ApJL* 274, L83
- Mundt, R. Stocke, J., & Stockman, H. S. 1982,
ApJL 265, L71
- Nolan, C. A., Salmeron, R., Federrath, C.,
Bicknell, G. V., & Sutherland, R. S. 2017,
MNRAS 471, 1488

- Osterbrock, D. E. 1989, in *Astrophysics of Gaseous Nebulae and Active Galactic Nuclei*, (Mill Valley, CA:University Science Books), p. 208
- Raga, A. C., de Gouveia Dal Pino, E. M., Noriega-Crespo, A., Mininni, P. D., & Velázquez, P. F. 2002, *A&A* 392, 267
- Raga, A. C., Riera, A., Masciadri, E., Beck, T., Böhm, K.-H. & Binette, L. 2004, *AJ* 127, 1081
- Reipurth, B. Heathcote, S. Yu, K. C., Bally, J., & Rodríguez, L. F. 2000, *ApJ* 534, 317
- Reipurth, B., Raga, A. C., & Heathcote, S. 1996, *A&A* 311, 989
- Schwartz, R. D. 1975, *ApJ* 195, 631
- Slavin, J. D., Dwek, E., & Jones, A. P. 2015, *ApJ* 803, 7
- Solf, J., Böhm, K.-H., & Raga, A. C. 1986, *ApJ* 305, 795
- Suzuki-Vidal, F., Lebedev, S., Ciardi, A., Pickworth, L. A., Rodriguez, R., Gil, J. M., Espinosa, G., Hartigan, P., Swadling, G. F., and Skidmore, J. 2015, *ApJ* 815, 96
- Tielens, A. G. G. M., McKee, C. F., Seab, C. G. & Hollenbach, D. J. 1994, *ApJ* 431, 321
- Williams, R. E. 1973, *MNRAS* 164, 111